Enhancement of charge photogeneration and transport via an internal network of Sb_2Se_3/Cu_2GeSe_3 heterojunctions

Xianghua Zhang,Yang Xu,Qianhong Shen, Bo Fan, Xusheng Qiao, Xianping Fan*, Hui Yang, Qun Luo, Laurent Calvez, Hongli Ma, Michel Cathelinaud, Jean-Jacques Simon*

Prof. Xiang-Hua Zhang, Dr. Bo Fan, Yang Xu, Dr. Laurent Calvez, Dr. Hongli Ma, Dr. Michel Cathelinaud,
Laboratory of glasses and ceramics, Institute of Chemical Science UMR CNRS 6226, University of Rennes 1, 35042 Rennes, France
E-mail: fanb07@hotmail.com

Dr. Qianhong Shen, Prof. Xusheng Qiao, Prof. Xianping Fan, Prof. Hui Yang, Dr. Qun Luo,
State Key Laboratory of Silicon Materials, Department of Materials Science & Engineering, Zhejiang University, Hangzhou 310027, P.R. China
Email: fanxp@zju.edu.cn

Prof. Jean-Jacques Simon
Aix Marseille Université, IM2NP UMR CNRS 7334, 13397 MARSEILLE Cedex 20, France

Supplementary information

1. AFM surface potential measurement

Figure S1 displays the histogram of AFM surface potential for the base glass before and after ceramisation. It can be seen that the surface potential of the sample is decreased after crystallization, and the glass-ceramic achieves a relatively high conductivity at the same time. Therefore, it can be deduced that the conductive region has lower surface potential than the non (or poorly)-conductive region in the same image for this system.

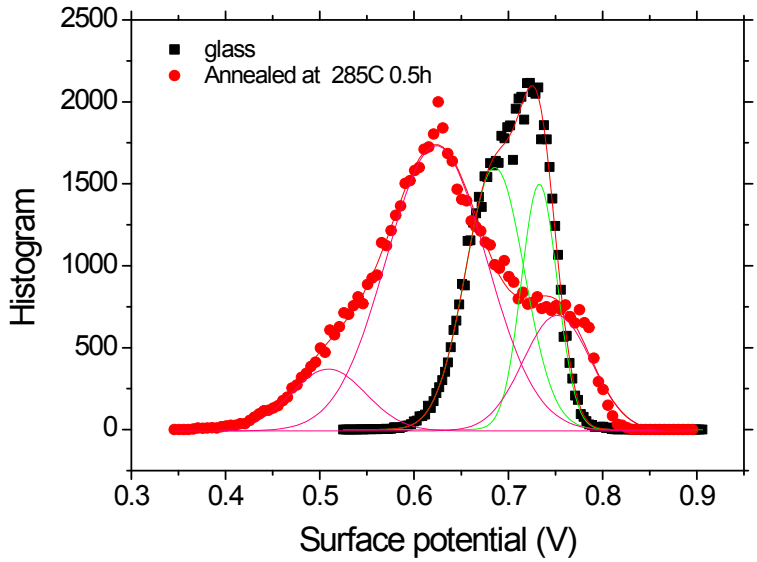

Figure S1 Histogram of AFM surface potential for the base glass before and after ceramisation.

Figure S2 shows the typical AFM surface potential images of some representative glass-ceramics. It can be seen from the Figure S2(a), for a non conductive glass-ceramic, that the high surface potential regions interconnect and form a network, whereas the low surface potential regions separately exist in the network. Based on the previous results, it can be clearly seen that the conductive microdomains (low surface potential regions) are separated by the non-conductive phase (high surface potential regions), so this glass-ceramic show a conductivity of around 10^{-8} $\Omega^{-1}cm^{-1}$. On the contrary, for the glass-ceramic with high conductivity, the high surface potential regions and the low surface potential regions form an interpenetrating network. Consequently, although there still exist non-conductive phase (high surface potential regions) in the glass-ceramic, the charge carriers can be transported through the interconnected conductive microdomains (low surface potential regions), leading to a relatively high conductivity.

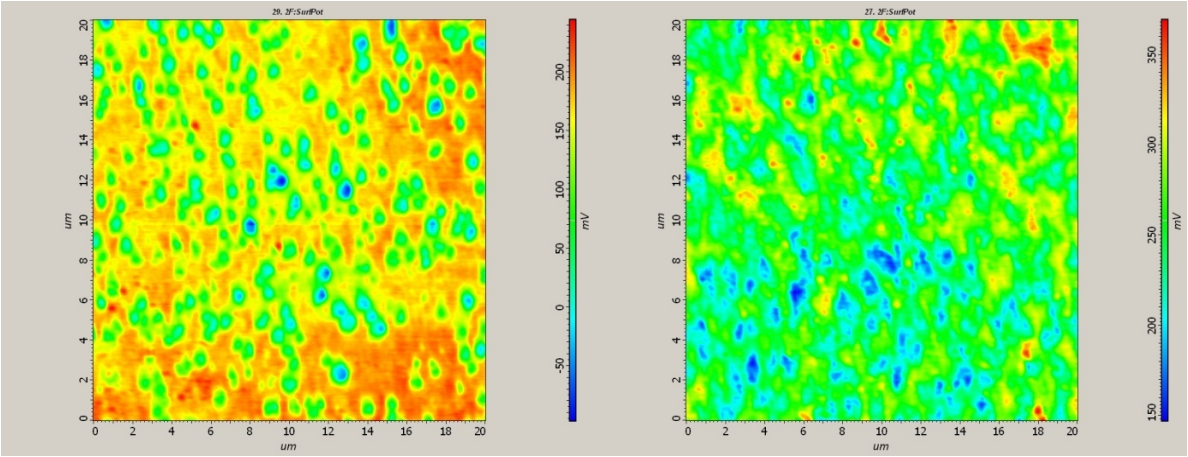

Figure S2 The typical AFM surface potential images of the glass-ceramics with different conductivity (a) 10^{-8} $\Omega^{-1}cm^{-1}$; (b) 10^{-2} $\Omega^{-1}cm^{-1}$.

2. Photo-electrochemical performance of the thin films

Since more intense photocurrent can be obtained when the thickness is reduced. As a preliminary attempt, we've studied the PEC properties of $40GeSe_2$-$40Sb_2Se_3$-20CuI glass-ceramic thin films.

The thin films were fabricated by co-sputtering with a radio-frequency magnetron sputtering system Plassys MP600s. Two targets, $50GeSe_2$-$50Sb_2Se_3$ and CuI, were used,. Firstly, the glassy thin films were deposited on the TiW/slide glass substrate (φ11 mm). The metallic TiW layer was used as the back contact. The deposition parameters are listed in Table S1. EDS analysis confirms that the composition of the thin films is close to $40GeSe_2$-$40Sb_2Se_3$-20CuI. Then the thin films were annealed in the silica tube connected to a turbo molecular pump. The annealing temperature was 280°C and the duration was 1hour. The XRD pattern of the annealed thin film (Figure S3(a)) shows that crystalline phases Sb_2Se_3 and Cu_2GeSe_3 are formed. The typical morphology of the annealed thin films is shown by cross-section SEM image in Figure S3(b). Rod-like crystals can be identified in the thin film. This morphology is similar to that of the bulk glass-ceramics.

Table S1 Deposition parameters of the glassy thin films

Background vacuum [mbar]	Power on $50GeSe_2$- $50Sb_2Se_3$ [W]	Power on CuI [W]	Work pressure [mbar]	Debit of **Ar** [sccm]
10^{-7}	14	11	0.015	50

The characterization of the photo-electrochemical performance of the annealed thin films is similar to the bulk samples: The measurement was based on 3-electrode method. Ag/AgCl standard electrode was used as the reference electrode, Pt as the counter electrode and the sample as the working electrode. Two different aqueous electrolytes were used: $LiClO_4$

solution (0.5 mol/L) and $Eu(NO_3)_3$ solution (0.1 mol/L $Eu(NO_3)_3$, 0.25 mol/L $K(NO_3)_3$, pH~2.0). An AUTOLAB METROHM potentiostat and a 150 W tungsten halogen lamp with a power density of 200 W/m^2 were used to record the current-voltage (I-V) characteristics under darkness and illumination.

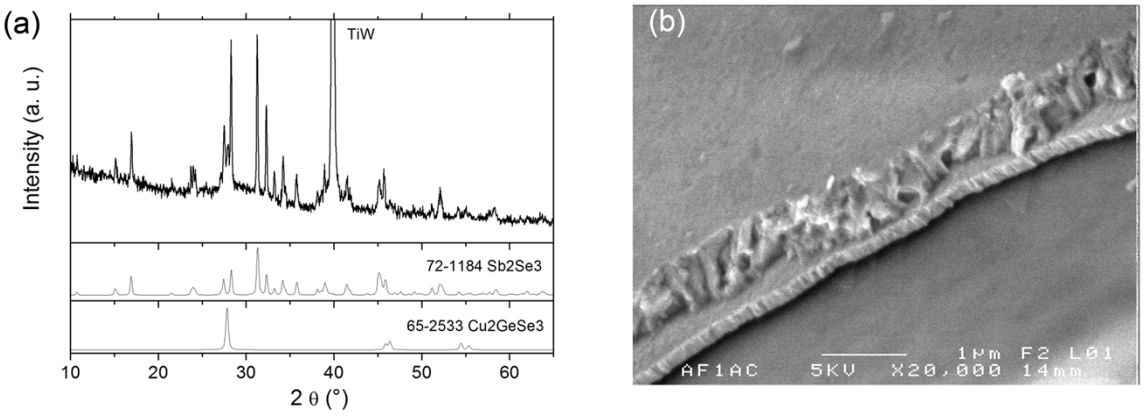

Figure S3. (a) XRD pattern of the annealed thin film, showing that the thin film consists of Sb_2Se_3 and Cu_2GeSe_3. (b) SEM image of the annealed thin films. Rod-like crystals can be identified in the thin film.

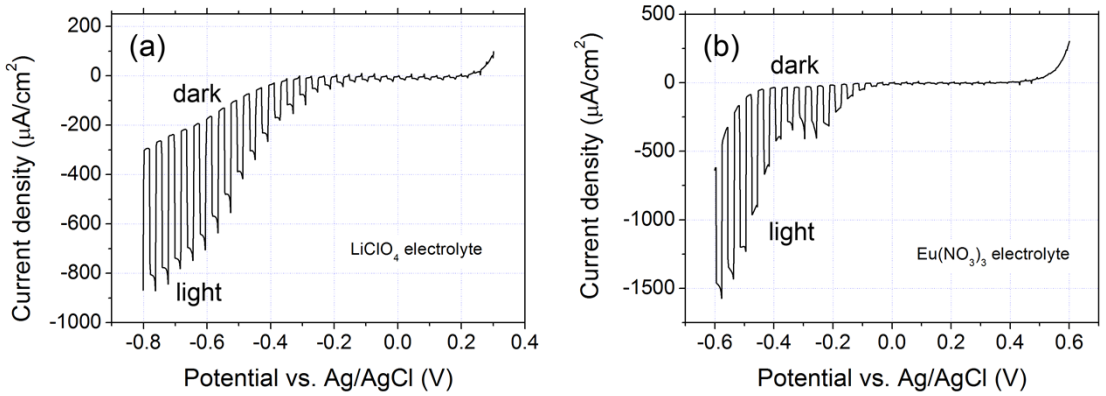

Figure S4. PEC measurement results of the annealed thin films under a chopped light source (200 W/m^2). (a) $LiClO_4$ electrolyte; (b) $Eu(NO_3)_3$ electrolyte.

Figure S4 presents the PEC measurement results of the annealed thin films in the two electrolytes. For the dark current, in Eu^{3+} electrolyte, cathodic current increases quickly at about -0.4 V vs. Ag/AgCl. This is due to the reduction of Eu^{3+} ions. No significant cathodic dark current in $LiClO_4$ electrolyte is observed because there is no suitable redox in this potential range.

The maximum photocurrent of the annealed thin films in the $LiClO_4$ electrolyte and $Eu(NO_3)_3$ eletrolyte are 527 μA/cm^2 (-0.76 V versus Ag/AgCl reference electrode) and 1100

$\mu A/cm^2$ (-0.53V versus Ag/AgCl reference electrode) respectively. These values are significantly improved in comparison with those of the bulk samples, approaching the application requirement. This improvement could be attributed to the fact that a smaller thickness in the thin films reduces the transport distance of the photo-generated charge carriers, thereby reducing the recombination possibility.

3. Photocatalysis study on the glass-ceramic powders

Figure S5 illustrates the UV-vis absorption spectra of methyl orange (MO) solutions photocatalytic degraded by the glass-ceramic for different times. It can be seen that the absorption peak of the initial MO solution shifts from its characteristic value of 464 nm to 470 nm, which may be due to a detection error generated by the relatively high concentration of MO solution, leading to a very high absorption and a very low signal level. The absorption peak of MO solution at 464 nm is associated with the azo bond (–N=N–) and is asymmetric. The broad absorption peak can be deconvoluted into two peaks centred at 464 nm and 443 nm (as shown in Figure S5). This peak centred at 443 nm is attributed to a reverse photo-isomerization of the azobenzene compound, namely, an azobenzene molecule will change from thermodynamically stable trans structure (E-type) to cis structure (Z-type) under excitation of visible light. The absorption peak centred at 276 nm is due to benzene charge-transfer absorption.

With the progress of the photocatalytic reaction, the absorption peaks centred at 464 nm, 443 nm and 276 nm decrease gradually, and a new absorption peak ranged from 228 nm to 250 nm appears simultaneously, indicating that some intermediates may be generated. This new absorption peak can be deconvoluted into two peaks located at 228 nm (226 nm) and 250 nm, which probably correspond to 4-hydroxybenzenesulfonic acid sodium and 4-dimethylaminophenol respectively.

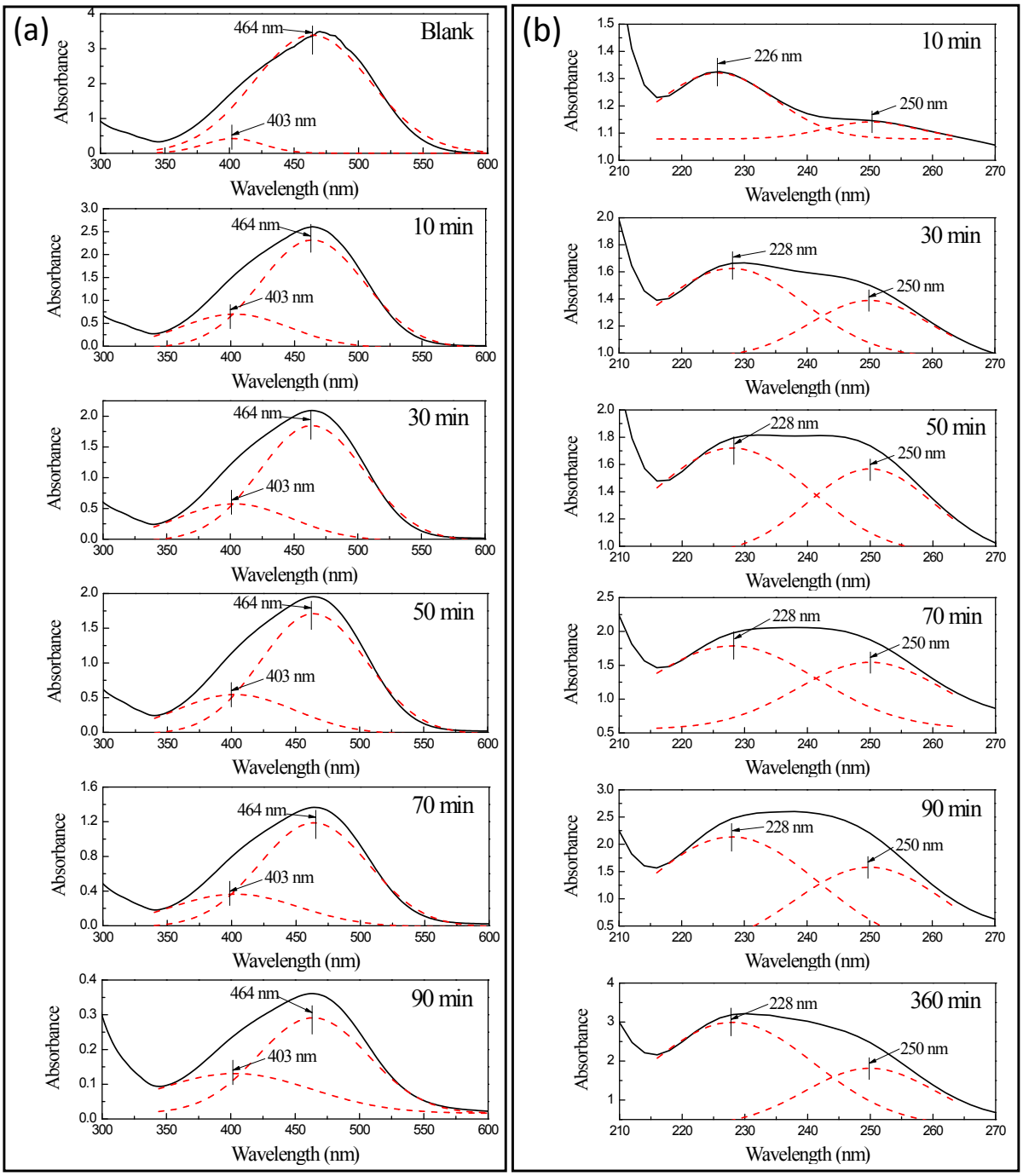

Figure S5. Evolution and peak fitting of UV-vis absorption spectra of MO solutions before and after photocatalytic reaction for different times.

The N-demethylation of MO will occur due to the attack of hydroxyl radicals on the N,N-dimethyl groups, generating sulfanilic sodium and N,N-dimethylamino aniline, leading to the consequent decolorization. However, these products cannot be detected in the UV-vis absorption spectra ranged from 210 nm - 600 nm as its maximum absorption wavelength is shorter than 200 nm. With the N-demethylation of MO, the hydroxylation with deamination

of the former two products occurs simultaneously, leading to the formation of 4-hydroxybenzenesulfonic acid sodium and 4-dimethylaminophenol, which have characteristic UV-vis absorption peaks at 228 nm and 251 nm respectively. These results are in good agreement with the deconvolution of the absorption peak. Therefore, the amount of these two intermediates increases with the photocatalytic reaction time, which is illustrated by the increase of the corresponding absorption peaks (as shown in Figure S5). After 6 hours of photocatalytic reaction, the absorption intensity at 228 nm increases more obviously. This is likely because a hydroquinone (the most hydroxylated direct product) is produced from the degradation of 4-hydroxybenzenesulfonic acid sodium and 4-dimethylaminophenol. Hydroquinone has a maximum absorption peak of 223 nm, leading to the shift of the total absorption peak to shorter wavelength region. Therefore, the likely photocatalytic degradation pathway for MO in this reaction system can be proposed as shown in Figure S6. The glass-ceramic photocatalyst exhibits a good oxidative deamination ability and its photocatalytic reaction process is different from that of most other photocatalysts reported before.

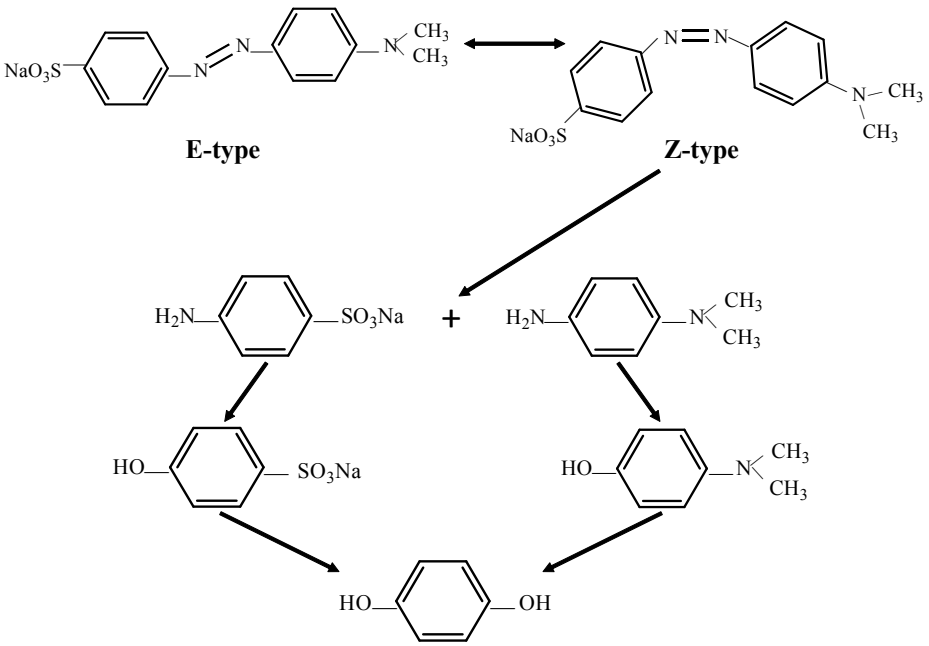

Figure S6. Main pathways proposed for MO photodegraded by the glass-ceramic under visible light.